Surface obstacles in pulsatile flow

Ian A. Carr, Michael W. Plesniak

Department of Mechanical and Aerospace Engineering
George Washington University
800 22nd St. NW Washington, DC 20052
icarr@gwu.edu, plesniak@gwu.edu

ABSTRACT

Flows past obstacles mounted on flat surfaces have been widely studied due to their ubiquity in nature and engineering. For nearly all of these studies, the freestream flow over the obstacle was steady, i.e. constant velocity, unidirectional flow. Unsteady, pulsatile flows occur frequently in biology, geophysics, biomedical engineering, etc. Our study is aimed at extending the comprehensive knowledge base that exists for steady flows to considerably more complex pulsatile flows. Characterizing the vortex and wake dynamics of flows around surface obstacles embedded in pulsatile flows can provide insights into the underlying physics in all wake and junction flows. In this study we experimentally investigate the wake of two canonical obstacles: a cube and a circular cylinder with an aspect ratio of unity. Our previous studies of a surface-mounted hemisphere in pulsatile flow are used as a baseline for these two new, more complex geometries. Phase-averaged PIV and hot-wire anemometry are used to characterize the dynamics of coherent structures in the wake and at the windward junction of the obstacles. Complex physics occur during the deceleration phase of the pulsatile inflow. We propose a framework for understanding these physics based on self-induced vortex propagation, similar to the phenomena exhibited by vortex rings.

INTRODUCTION & BACKGROUND

The study of fluid flow around surface-mounted obstacles has a long history in fluid dynamics. From mussels embedded in a river bed to flow around buildings, the occurrences of surface obstacles in nature and engineering are numerous (Hajimirzaie & Buchholz, 2013; Yang *et al.*, 2011). In nearly all reported studies, the freestream flow around the obstacle in question has been steady, i.e. not time-varying. On the other hand, pulsatile flows often occur in biological and geophysical flows and present a challenging set of flow conditions. The aim of this work is to fill a gap in the knowledge base by extending previous studies on steady flow over surface obstacles to pulsatile flow.

The present study is focused on obstacles of aspect ratio near unity. Obstacles of this type are known to produce highly three-dimensional wakes, e.g. Sumner et al. 2013 showed that surface-mounted cylinders with an aspect ratio of 3 or less produce three-dimensional wakes. This is our area of interest. A recent review of surface obstacle wakes and arch-type recirculation vortices can be found in Gonçalves *et al.* (2015).

In our previous studies we found complex and interesting fluid dynamics around a surface-mounted hemisphere in *extremely pulsatile* flow. We define extremely pulsatile flow as flow in which magnitude of the freestream oscillations is as large as the mean flow velocity. We studied the behavior the arch-type recirculation vortex found in the wake of the hemisphere. Figure 1 is a schematic representation of the arch recirculation vortex, as well as the other relevant flow features in the averaged wake of a surface-mounted hemisphere in steady flow. This representation was constructed from PIV velocity field data in multiple planes.

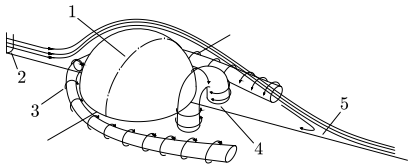

Figure 1. Averaged flow structures around a surface-mounted hemisphere in steady flow. 1: line of separation 2: incoming boundary layer 3: horseshoe vortex 4: arch recirculation vortex 5: boundary layer reattachment (Carr & Plesniak, 2016).

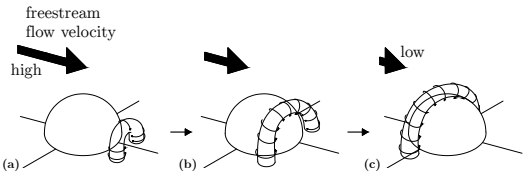

Figure 2. Schematic representation of the arch vortex propagation during inflow deceleration (Carr & Plesniak, 2016).

In Carr & Plesniak 2016, we observed that the arch recirculation vortex propagates upstream during the *deceleration* phase of the pulsatile inflow profile. Figure 2 depicts the upstream propagation.

To explain this motion we invoke the analogy to the self-induced propagation exhibited by vortex rings. We used an expression developed by P.G. Saffman for the theoretical propagation velocity of a vortex ring (Saffman, 1970). Assuming an image vortex reflected through the base plane and using velocity field data from PIV measurements, the theoretical propagation velocity of the arch vortex was calculated. The result was within a factor of two of the observed propagation velocity. Self-induced propagation during the portion of the cycle when inflow velocity is low provides a compelling explanation for the unintuitive physics observed. For the details of this calculation and the rest of the study see Carr & Plesniak (2016).

In the present study, we investigate the effect of obstacle geometry. Namely, we investigate the dynamics of vortical structures around two distinct surface-mounted obstacle geometries: a circular cylinder of aspect ratio 1:1 as well as a cube. We investigate the flow fields experimentally, and propose a mechanistic explanation for the (surprising) vortex dynamics observed based on the same self-induced propagation. These results are compared with each other, as well as our previously published work on a wall-mounted hemisphere in pulsatile flow (Carr & Plesniak, 2016).

Cubes and low-apsect ratio circular cylinders have been reported to produce arch-type recirculation vortices. The choice of the geometries was informed by previous depictions of their associated wake structure. Figure 3 shows an arch recirculation vortex

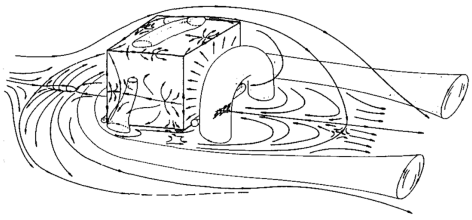

Figure 3. Averaged flow structures around a surface-mounted cube in steady flow (Martinuzzi & Tropea, 1993).

s

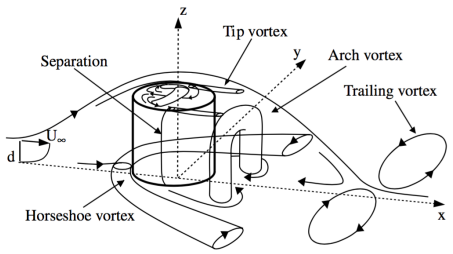

Figure 4. Averaged flow structures around a surface-mounted, low aspect ratio circular cylinder in steady flow (Pattenden *et al.*, 2005).

in the wake of a cube from Martinuzzi & Tropea (1993). Figure 4 shows a similar arch-type structure in the wake of a low aspect ratio circular cylinder depicted Pattenden *et al.* (2005). Both of these flows exhibit arch-type recirculation vortices very similar to those observed in the wake of the hemisphere in pulsatile flow (Carr & Plesniak, 2016). This raises several interesting questions. Will these arch vortices react the same way to extremely pulsatile flow? Will the additional complexity of these geometries impede or enhance the vortex propagation associated with the hemisphere case? Is the upstream propagation unique to the hemisphere or applicable to all surface-mounted obstacles in extremely pulsatile flow?

EXPERIMENTAL METHODS

All experiments were performed in a low-speed wind tunnel using two-dimensional particle image velocimetry (PIV) and hot-wire anemometry. Figure 5 is a schematic representation of the wind tunnel, which has a freestream turbulence intensity of 0.7% (Wolochuk, 1994). A set of rotating vanes positioned at the test section's exit were used to produce the pulsatile inflow velocity profile shown in Figure 6. When the shutters are perpendicular to the freestream streamlines 97% of the test section's cross section is blocked. When they are parallel to the freestream streamlines only 11% of the test section is blocked. For the results reported herein the shutters were rotated at a constant velocity with a frequency of 2Hz. The inflow waveform is highly repeatable with an average deviation over 100 cycles of 0.7% of the amplitude and 2.1% of the frequency.

The PIV system consists of a New Wave Research Nd:YAG laser, a TSI PowerView Plus 4MP camera with a Nikkor 105mm micro lens, a TSI LaserPulse synchronizer, and a LaVision Rocket Fogger which produces monodispursed, 1 micron aerodynamic diameter fog particles consisting of a water and glycerine mixture. All PIV images were captured using TSI Insight 4G software. Vector fields are calculated from the raw PIV images using LaVision DaVis 8.3 software. The constant temperature anemometer (CTA) is a Dantec MiniCTA with a platinum wire probe, which feeds data through a National Instruments data acquisition board. The hotwire is calibrated using a Pitot static probe attached to a Scanivalve DSA-3217 pressure transducer before each use.

Four PIV fields of view (FOV) were investigated: 1) a large field side view at z/D = 0.0, 2) a detailed side view focused on the top surface of the obstacles at z/D = 0.0, 3) a large scale top view just above the obstacle's crest at y/D = 1.1, 4) a top view intersecting the obstacle at y/D = 0.5. The PIV image capture process was synchronized with the motion of the rotating shutters using an optical sensor to obtain phase-averaged velocity fields. Vortices were identified in the vector fields by swirling strength (λ_{ci}) contours (Zhou *et al.*, 1999). The CTA was used to monitor the bulk inflow profile and used to obtain highly time-resolved frequency data in the wake of the obstacle.

RESULTS & DISCUSSION

Figures 1, 3, and 4 all depict recirculation vortices of similar morphology for *steady flow*. The regularity of steady flow allows these vortices to remain relatively stationary. Our investigations revealed that'd a similar regularity exists in the acceleration phase of an extremely pulsatile waveform. We posit Figures 1, 3, 4 are just as relevant for the acceleration phase of an extremely pulsatile flow. We must then determine what occurs during inflow deceleration. In this section we will characterize the cube and cylinder using a similar approach as was used on the hemisphere.

Cube: pulsatile flow features

Figure 7 shows top and side view velocity vector fields with swirling strength contour underlays at four phases: time* = 0.0, 0.38, 0.5, 0.61 taken at the cube centerline plane (side view) and just above the top surface (top view). Figure 8 shows a top view at time* = 0.0 taken at the half height of the cube. In all realizations the axes are normalized by the characteristic length of the obstacle, D. From Figures 7 and 8 it is clear the arch vortex exists in the wake of the cube at time* = 0.0. The combination of these two suggests a structure very similar to that depicted by Martinuzzi & Tropea (Figure 3).

Figure 9 is a schematic representation developed from the flow fields in Figure 7. The aim of Figure 9 is not only to clarify the complexity of the flow around a cube in deceleration, but also to provide comparison to Figure 2. Figure 9a is representative of all of the acceleration phase of the inflow cycle and agrees closely with Martinuzzi's representation, shown in Figure 3. It should be noted not all of the structures observed in flow are shown in the schematic, only the largest.

In Figure 7 three phases in the deceleration portion of the cycle are shown: early, mid, and late deceleration at time* = 0.0, 0.50, and 0.63, respectively. During early deceleration (time* = 0.38 in Figure 7) the free shear layer begins to lift off the surface vertically and symmetrically expand in the spanwise direction. This greatly increases the total volume of the separation bubble along with the arch vortex inside it. Recall the top view plane in Figure 7 is located at y/D = 1.1. During early deceleration the legs of the arch vortex become visible in the top view. These flow features are shown in Figure 9b. A small, but detectable, junction-type flow forms on the *leeward* cube-surface interface. This is represented as a small concentration of high swirling strength at x/D = 0.0, y/D = 0.5. This is the signature of the head of a horseshoe vortex with legs, which wrap around either side of the obstacle.

Mid-deceleration (time* = 0.50) is the most complex portion of the cycle. None of the primary vortex structures present have yet broken down. In the side view of Figure 7 the arch vortex has propagated vertically with its core at y/D $\approx$ 1.4. Just upstream of the primary arch vortex there is a packet of high velocity flow near the

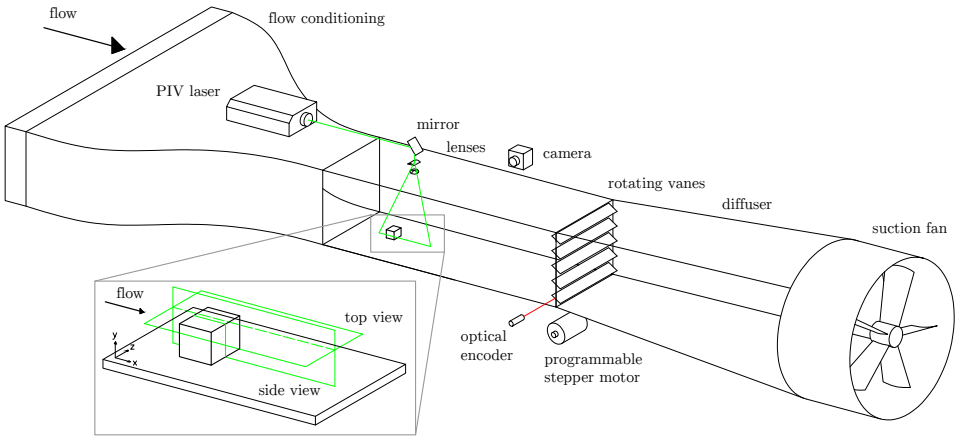

Figure 5. Schematic representation of wind tunnel used in all experiments. Detail of PIV planes at z/D = 0 and y/D = 1.1 around surface-mounted obstacle.

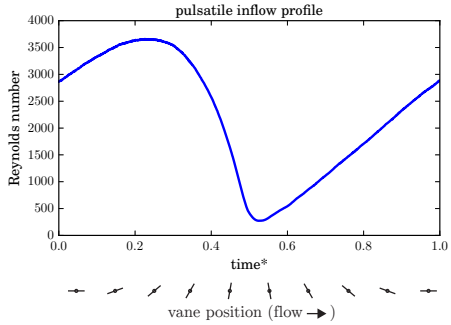

Figure 6. Inflow profile produced by rotating vanes at a constant angular velocity.

top, leeward corner of the cube. Figure 10 shows a detailed view of the this region. When viewed from the side this flow is forced through a small opening, between the cube's corner and the head of the arch vortex, and subsequently accelerates. Interestingly, at this phase, this flow packet is the fastest moving fluid in the FOV with a velocity magnitude roughly double that of the freestream flow. As this packet of high velocity flow moves past the top, leeward corner of the cube another shear layer and small, counter-rotating recirculation vortex is formed. This recirculation vortex is represented by a concentration of swirling strength at x/D = 0.3, y/D = 1.2. This is a novel phenomenon not previously reported; whereas the other vortices observed in Figure 7 have traceable origins found in Figure 3, the recirculation vortex does not — it is formed *during* deceleration. This new structure counter-rotating to the main arch vortex is shown in Figure 9c. Lastly, during mid-deceleration, a third vortex appears with its head at x/D = 0.0, y/D = 1.4 and it's legs at x/D = -0.2 and z/D = $\pm$0.8. This third, forward-most vortex originates from the local recirculation vortex on the top surface of the cube and is similarly signed to the primary arch vortex.

Finally, late deceleration (time* = 0.61) is when the structures begin to lose coherence or dissipate. The smaller scale structures at time* = 0.50 are considerably less organized in the top view at time* = 0.61. However, in the side view the head of the primary arch vortex is still present and coherent. The vortex birthed during deceleration atop of the cube (now at x/D $\approx$ 0.0, y/D $\approx$ 1.3) is also still present, albeit less organized. At this phase, the primary, large-scale arch vortex has propagated to nearly the upstream most point in its trajectory. It almost reaches the centerline of the cube (x/D = 0.0) before being convected downstream by the freestream flow. Lastly, the junction vortex at the cubes leeward face is still visible at this phase.

After time* = 0.65, the arch recirculation vortex no longer has sufficient self-induced velocity to propagate upstream and is convected downstream by the freestream flow. At time* = 0.7 the flow starts to accelerate and the arch vortex quickly dissipates in the freestream. However, the junction vortex at the leeward face of the cube remains intact well into acceleration. It exists until time* = 0.81, after which the freestream flow is entirely dominant. The flow structures represented in Figure 3 begin to form again and the cycle repeats.

Cylinder: pulsatile flow features

The general steady flow features in Figures 3 and 4 are largely similar. Steady flow around both give rise to a large scale, arch-type recirculation vortex and small scale, local recirculation vortices on their flat surfaces. One primary difference is the cube is comprised of multiple flat surfaces, which breed multiple small scale recirculation vortices, while the cylinder only has one flat top. Not surprisingly the flow features in pulsatile flow are also similar.

Figure 11 shows a set of phase-averaged velocity vector fields with swirling strength contour underlays. Four phases are represented, the first being mid acceleration at time* = 0.0, which is representative of the entire acceleration portion of the cycle as the flow structures do not vary significantly. The three subsequent phases plotted are early mid, and late deceleration at time* = 0.38, 0.50, and 0.61, respectively.

In Figure 11 at time* = 0.0 the head of the recirculation vortex can be seen in the wake of the cylinder. The vortical structures do not pierce the top view plane and the flow through this plane is largely undisturbed. The intensity of swirling strength nearly doubles throughout acceleration, but the repetitive vortical structure remains spatially stationary. At time* = 0.38 (Figure 11c & d) the large-scale wake recirculation zone widens and lifts up, becoming visible in the top view at x/D = 1.0 and z/D = $\pm$0.5. The local recirculation zone atop the cylinder lifts up and is now visible in the top view at x/D = 0.0, z/D = $\pm$0.25. Correspondingly, the beginning of the formation of the counter rotating vortex pair produced during deceleration (as seen in the cube). The early formation of

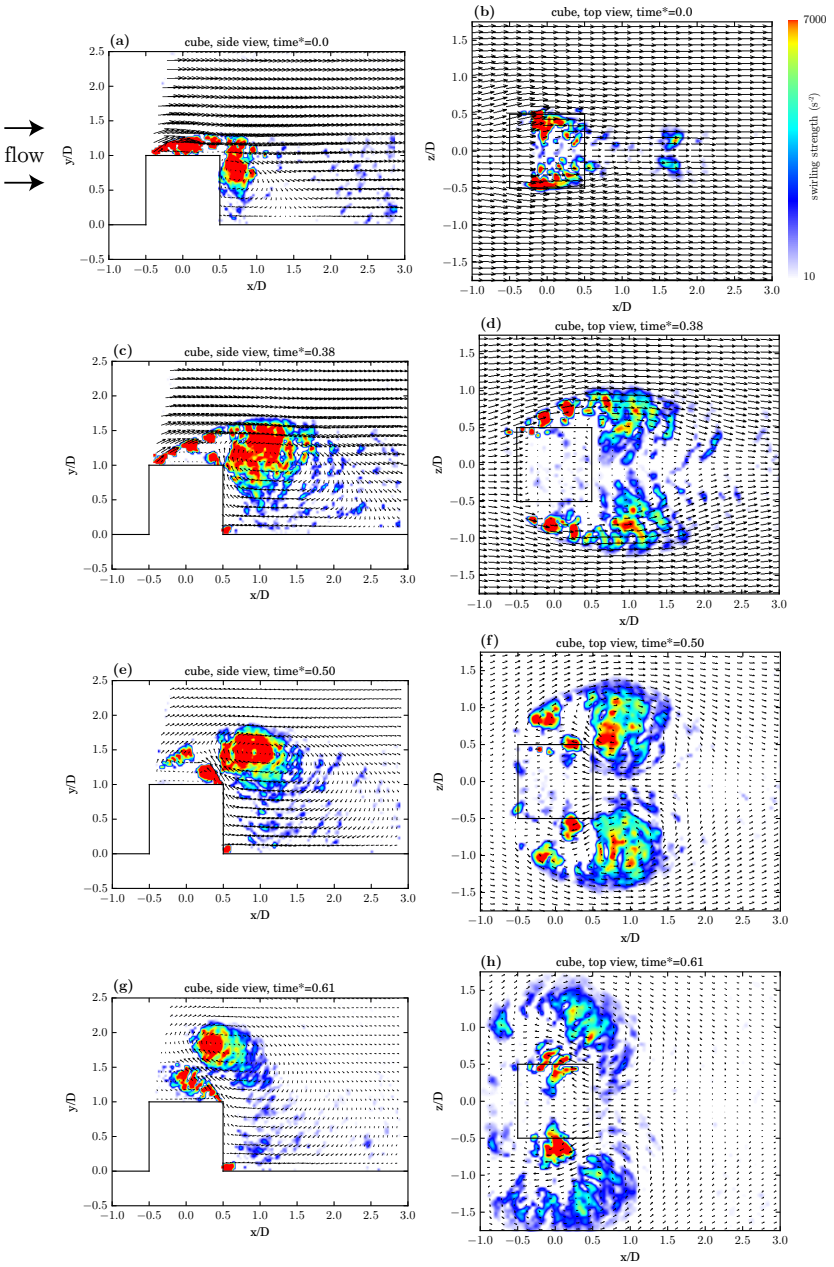

Figure 7. Phase-averaged velocity vector fields superimposed on swirling strength contour underlays proximal to a surface-mounted cube at time* = 0, 0.38, 0.50, 0.61. Freestream flow is from left to right.

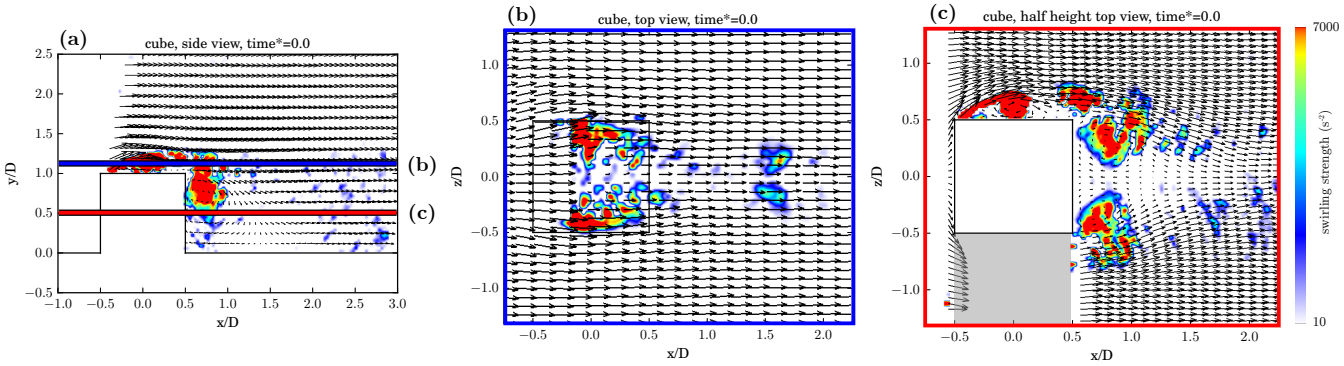

Figure 8. Phase-averaged velocity vector fields with swirling strength underlays at time* = 0.0. (a) Side view with vertical positions of the two top view planes (b) Top view at y/D = 1.1 (c) Top view at y/D = 0.5. Freestream flow is from left to right. Grey area indicates laser shadow.

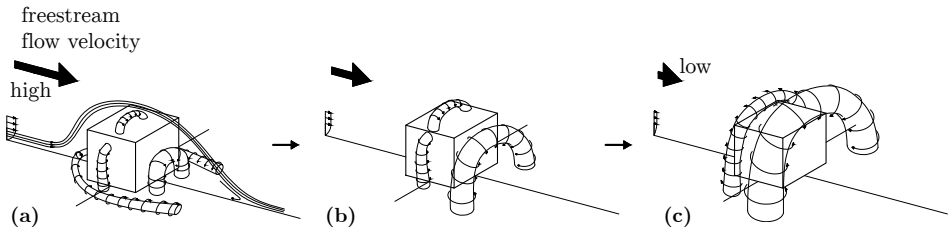

Figure 9. Schematic representation of the flow structures around a surface mounted cube during accelerating flow (a), early deceleration (b), and late deceleration (c).

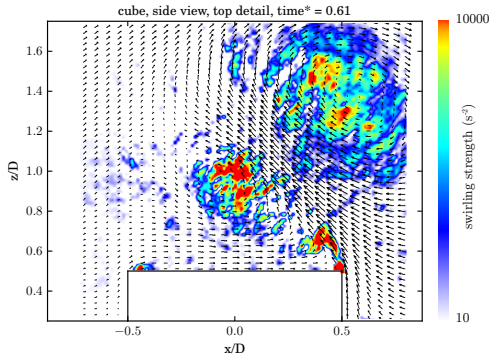

Figure 10. Velocity vector field with swirling strength contour underlay side view focused on the top of the cube at time* = 0.50. Freestream flow is from left to right.

the deceleration-birthed vortex at x/D = 0.4, z/D = $\pm$0.3.

As with the flow around the cube, mid deceleration (time* = 0.50) is the most complex part of the cycle. The legs of the arch recirculation vortex are located at x/D = 1.0. The local recirculation originating from the top of the cylinder gives rise to the upstream-most set of vortex structures visible at x/D = -0.4. Just downstream, the counter rotating deceleration-birthed vortices occur at x/D = 0.3. The morphology and relative size of each vortex pair at time* = 0.50 the wakes of the cube and cylinder most differentiate. Finally, at time* = 0.63 the structures start to dissipate. The two sets of vortices atop the cylinder are no longer distinct. The arch recirculation vortex has nearly reached its forward most point at x/D $\approx$ 0.2. After time* = 0.65, both vortex pairs are convected downstream and lose coherence at x/D = 8.

Primary vortical structures

Our prior study of a surface-mounted hemisphere provided the basis for understanding the obstacles featured in the present study. Compared to the obstacles studied here, a surface mounted hemisphere is considerably more streamlined and produces only a single recirculation vortex in its wake. The sharp edges of the cube and cylinder give rise to multiple recirculation regions, i.e. on top and sides in addition to the large scale recirculation behind.

In steady flow, this wake recirculation vortex is confined below the free shear layer in the wake of the obstacle and is often accompanied by vortex shedding from the free shear layer. Extremely pulsatile flow produces the complex vortex dynamics around the cube and cylinder represented in Figures 7 and 11, respectively. During deceleration the velocity of the freestream flow and its influence is greatly diminished. Meanwhile, the velocity field in the wake of the obstacle remains relatively constant. Thus, while the freestream flow decelerates rapidly, the recirculation vortex is "shielded" by the obstacle and maintains its rotational velocity. Due to a sudden regime shift, from one where the *freestream fluid flow is dominant* to one in which the *self-induced velocity dominates*, ***the recirculation vortex propagates upstream*** under its own self-induced velocity field. This regime shift is the first-order mechanism that we reported for the large scale vortex dynamics (Carr & Plesniak, 2016).

Because the hemisphere only had one recirculation zone there was only one recirculation vortex present, and therefore only one propagating vortex during inflow deceleration. The cube and cylinder have multiple recirculation zones which give rise to multiple recirculation vortices. During inflow deceleration the multiple recirculation vortices propagate and interact with each other and with nearby boundaries.

The existence of the recirculation zones during acceleration and subsequent upstream propagation of the associated vortices accounts for the dynamics of only two of the three sets of vortices visible in the top view for each obstacle. Unlike the other two, which are formed during inflow acceleration and persist into deceleration, this third vortex is *formed during deceleration*. This is a novel manifestation of the regime-switching scheme mentioned above. Observing flow around the obstacles from the side during inflow acceleration reveals that the free shear layer (above the corresponding recirculation vortex in the wake) is horizontally oriented, parallel to the wall. During deceleration when the freestream velocity becomes small the velocity field of the recirculation vortex dominates. The fastest flow is a packet moving in the positive Y-direction between the obstacle and the recirculation vortex. This packet of high velocity flow is pictured for the cube in Figure 8. It then moves up the rear face of the obstacle until it reaches the top of the obstacle, where another shear layer is produced. The recirculation region contains the third vortex at x/D = 0.0, y/D = 0.9 in Figure 8. In the side view this set of vortices is oppositely-signed from the other two vortex pairs (those originating from the recirculation regions).

From the experiments reported here it is clear the self-induced propagation of a recirculation vortex in extremely pulsatile flow is a robust feature and the upstream motion of the large-scale recirculation vortex in the obstacles wake is common to various obstacle geometries. The sharp corners of the cube and cylinder add complexity in two ways: multiple recirculation zones give rise to multiple propagating vortices, and a counter rotating vortex is created during deceleration.

CONCLUSION

The vortex dynamics arising from various surface obstacles immersed in a pulsatile freestream have been experimentally investigated. 2D-PIV and hot-wire anemometry techniques were used to measure the flow fields in a low-speed wind tunnel. A set of rotating vanes at the wind tunnel test section exit were utilized to produce the extremely pulsatile inflow waveform shown in Figure 6. Sets of vortical structures have been observed to form, evolve and de-

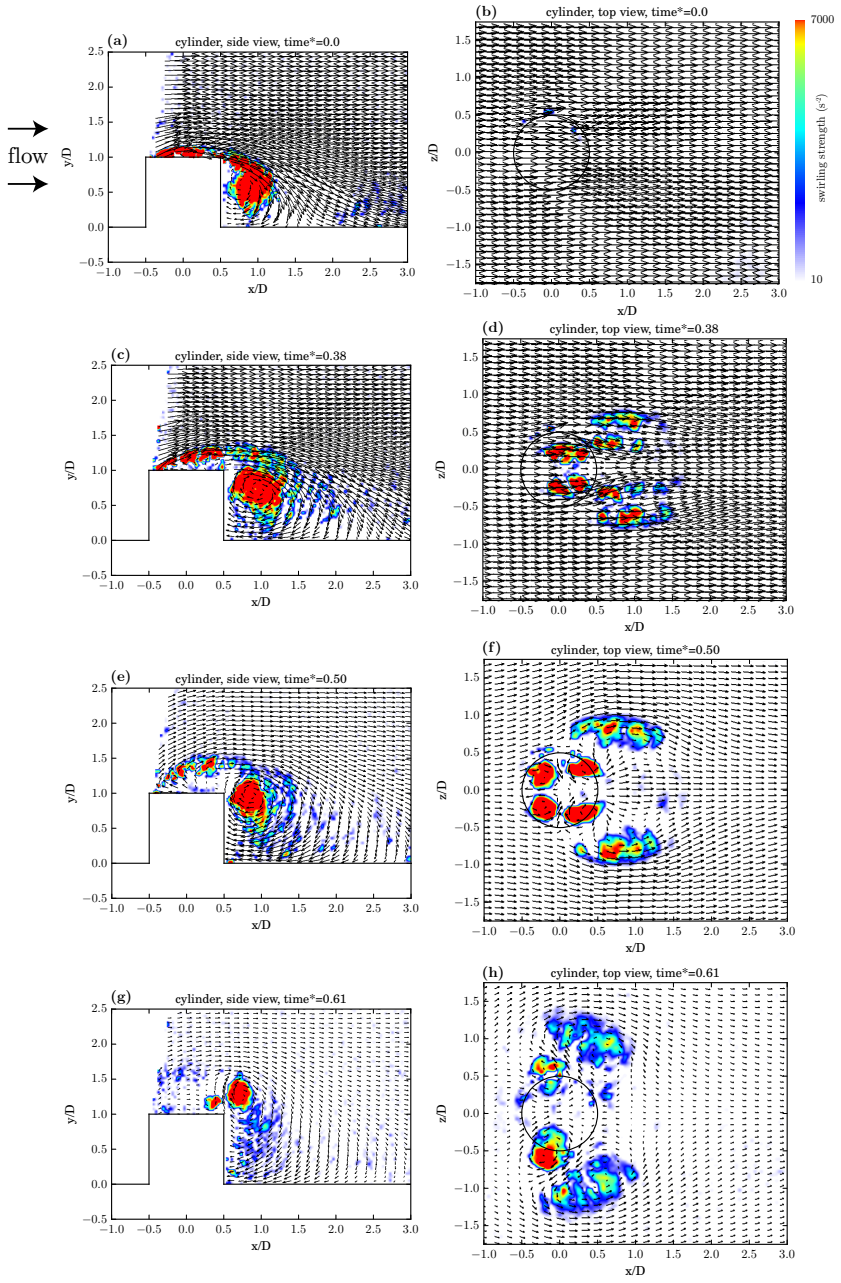

Figure 11. Vector field with swirling strength contour around a surface-mounted circular cylinder of aspect ratio 1:1 at time* = 0.0, 0.38, 0.50, 0.61.

cay in phase with the pulsatile freestream. The most dominant and largest of the structures, an arch-type recirculation vortex, occurs in all three geometries. Figures 7, 11, and 8 show cross sections of the arch recirculation vortex. During the deceleration phase of the extremely pulsatile inflow profile the arch recirculation vortex propagates upstream. The upstream propagation is attributed to the self-induced velocity field of the vortex as it was for our hemisphere case (Carr & Plesniak, 2016). In the case of the cube and cylinder, the sharp corners lead to added complexity. The localized recirculation regions on the flat surfaces of the cube and cylinder contain an averaged recirculation vortex during freestream flow acceleration. During deceleration, the localized recirculation vortices propagate upstream in a similar manner as the large-scale arch vortex does. Additionally a third vortex is produced during deceleration and rotates in the direction opposing the others. Figure 10 is a detail side view of the top of the cube at time* = 0.50 showing the formation of the third, counter-rotating vortex.

These results suggest that the self-induced upstream propagation mechanics of a wake vortex in extremely pulsatile flow is not geometry dependent. All low aspect ratio bluff bodies mounted on a surface in an extremely pulsatile freestream are expected to produce an arch vortex. The propagation of the arch vortex during deceleration does not appear to be impeded by obstacles. In all cases the vortex propagates to roughly the centerline of the obstacle before being convected downstream. The universality of this phenomenon greatly expands its scope and applicability to a wide range of engineering flows.

REFERENCES

Carr, Ian A. & Plesniak, Michael W. 2016 Three-dimensional flow separation over a surface-mounted hemisphere in pulsatile flow. *Experiments in Fluids* **57** (1), 9.

Gonçalves, R. T., Franzini, G. R., Rosetti, G. F., Meneghini, J. R. & Fujarra, A. L C 2015 Flow around circular cylinders with very low aspect ratio. *Journal of Fluids and Structures* **54**, 122–141.

Hajimirzaie, Seyed M. & Buchholz, James H. J. 2013 Flow dynamics in the wakes of low-aspect-ratio wall-mounted obstacles. *Experiments in Fluids* **54** (11), 1616.

Martinuzzi, R. J. & Tropea, C. 1993 The flow around surface-mounted, prismatic obstacles placed in a fully developed channel flow. *Journal of Fluid Engineering* **115**, 85–92.

Pattenden, R. J., Turnock, S. R. & Zhang, X. 2005 Measurements of the flow over a low-aspect-ratio cylinder mounted on a ground plane. *Experiments in Fluids* **39** (1), 10–21.

Saffman, P G 1970 The Velocity of Viscous Vortex Rings. *Stud. Appl. Math.* **49**, 371.

Wolochuk, M.C. 1994 Evaluation of Vortex Shedding Flow Meters for HVAC Applications. Master of science, Purdue University.

Yang, Zifeng, Sarkar, Partha & Hu, Hui 2011 An experimental study of a high-rise building model in tornado-like winds. *Journal of Fluids and Structures* **27** (4), 471–486.

Zhou, J., Adrian, R. J., Balachandar, S. & Kendall, T. M. 1999 Mechanisms for generating coherent packets of hairpin vortices in channel flow. *Journal of Fluid Mechanics* **387**, 353–396.